Int. J. Electrochem. Sci., 14 **(2019)** 2560 – 2573, doi: 10.20946/2019.03.67

International Journal of ELECTROCHEMICAL SCIENCE
www.electrochemsci.org

Numerical Simulation and Experimental Validation of the Erosion Behaviour of X65 Pipeline Steel under Different Flow Velocities and Sand Concentrations

Weimin Ma[1, 2], *Jihui Wang*[1, 2, *], *Qiushi Li*[2], *Dahai Xia*[2], *Wenbin Hu*[2]

[1] State Key Laboratory of Hydraulic Engineering Simulation and Safety, Tianjin University, Tianjin 300072, P R China
[2] Tianjin Key Laboratory of Composite and Functional Materials， School of Materials Science and Engineering, Tianjin University, Tianjin 300072, P R China
[*]E-mail: jhwang@tju.edu.cn

Received: 4 November 2018 / *Accepted:* 14 December 2018 / *Published:* 7 February 2019

The erosion behaviour of X65 pipeline steel in simulated formation water was investigated under different flow velocities and sand concentrations by using numerical simulation and experimental methods. In the numerical simulation, the geometry model was first built according to the erosion loop system in the experimental test, and then the shear stress transport (SST) *k-ω* turbulence model and the discrete phase model (DPM) were applied to simulate the fluid path and the erosion rate during the erosion process. In the experimental test, the erosion rate of X65 steel was determined under different flow velocities and sand concentrations by using a water-sand erosion loop system. The numerical simulation and experimental results showed that the erosion rate of X65 steel clearly increased with the increasing flow velocity and sand concentration, and there is good agreement between the numerical simulation erosion rate and the experimental results.

Keywords: erosion, numerical simulation, experimental validation, flow velocity, sand concentration

1. INTRODUCTION

Erosion or erosion–corrosion are the main failure modes for pipes and overflow components in the field of oil and gas production due to flow-induced corrosion. The erosion behaviour of materials not only is influenced by the characteristic of corrosion media (salt concentration, pH value, temperature, etc.) but also depends on the fluid flow parameters (such as flow velocity, particle concentration and impact angle) [1-3] and the particle parameters (such as particle size, hardness and shape) [4, 5]. Thus, there is great significance to reveal the effect of the erosion parameters on the erosion behaviour and

mechanism of materials.

For the erosion-corrosion of materials, experimental testing and numerical simulation methods are normally applied [6-12]. In the aspect of experimental tests, the erosion-corrosion behaviour of 3003 aluminium alloy in ethylene glycol-water solution was investigated by using the impingement jet system and rotating disk electrode methods, which indicated that the erosion-corrosion rate of aluminium alloy significantly increased with the increasing sand concentration and rotation speed [7, 8]. The erosion-corrosion behaviour of X52 steel under different flow velocities was investigated by a combination of the impinging jet apparatus and the electrochemical method, and the experimental results showed that the anodic current density of X52 steel in the water increased with the flow velocity [9]. In the aspect of numerical simulation, the symmetric geometry model and the standard k-ε turbulence model were applied to simulate the erosion behaviour of materials under different impact angles, and the velocity distribution plots of the water phase and the particle trajectories in diluted water-sand flows were well presented [10]. The pressure and erosion contours on the wall of the 90° elbow were predicted by using the standard k-ε model and the solid particle erosion model, and the maximum erosion was located near the area with maximum pressure [11]. By combining the numerical simulation and experimental test methods, Nguyen [12] analysed the erosion rate of SUS304 stainless steel in the water while containing sand under different operation times and flow velocities. It was found that the erosion rate by the numerical simulation method exhibited the same trend as the experimental results, but there was a large error between the numerical and experimental data.

In this work, the erosion behaviour of X65 pipeline steel in simulated formation water was investigated by using a water-sand loop system under different sand concentrations and fluid velocities. Then, the geometry model, shear stress transport (SST) k-ω turbulence model and discrete phase model (DPM) were applied to simulate the erosion behaviour and the erosion rate by using ANASYS Fluent software. By comparing the numerical result with the experimental data, the effects of the flow velocity and sand concentration on the erosion behaviour were discussed, and the simulation model for the erosion of X65 pipeline steel in simulated formation water could be validated.

2. EXPERIMENTAL

The erosion of X65 pipeline steel in simulated formation water was carried out in a homemade water-sand erosion loop system, which was composed of a control cabinet, screw pump, flow meter, sand feeder, solution tank, flowing jet and sample holder, as shown in Fig. 1. The flow velocity of water in the range of 5 to 20 m/s was adjusted by the rotation handle on the screw pump, and the sand concentration in water in the range of 0 to 0.2 wt.% was controlled by a sand feeder. The diameter of the flowing jet was 4 mm, and the distance and impingement angle between the jet and sample were fixed at 20 mm and 90°, respectively.

The chemical composition of X65 pipeline steel is shown in Table 1, and the simulated formation water was composed of NaCl, KCl, $CaCl_2$, Na_2SO_4, $MgCl_2{\cdot}6H_2O$ and $NaHCO_3$ components, as presented in Table 2 [13]. Before the erosion test, X65 steel samples with the dimensions of 20×15×4 mm^3 were abraded by silicon carbide paper (from 400# to 2000#) and were polished, cleaned and dried.

The weight of the samples was determined by using an electronic balance with an accuracy of 0.1 mg.

The erosion test of X65 steel was carried out in simulated formation water with the flow velocities of 11, 14 and 17 m/s and sand concentrations of 0.05%, 0.10% and 0.20% (wt.%). The duration of the erosion test is 6 hours. After the erosion test, the samples were cleaned and weighed. The erosion rate of the X65 pipeline steel was calculated by using the following formula:

$$v = \frac{m_0 - m_1}{S \cdot t} \quad (1)$$

where v is the erosion rate in kg/(m^2·h); m_0 is the mass weight before test (kg); m_1 is the mass weight after the erosion test (kg); S is the exposed surface area of sample (m^2); and t is the test duration (s). The surface morphology of the test sample was observed by scanning electron microscopy (SEM).

To compare with the numerical simulation results, the erosion tests of X65 steel were also performed in simulated formation water without sand particles under different flow velocities.

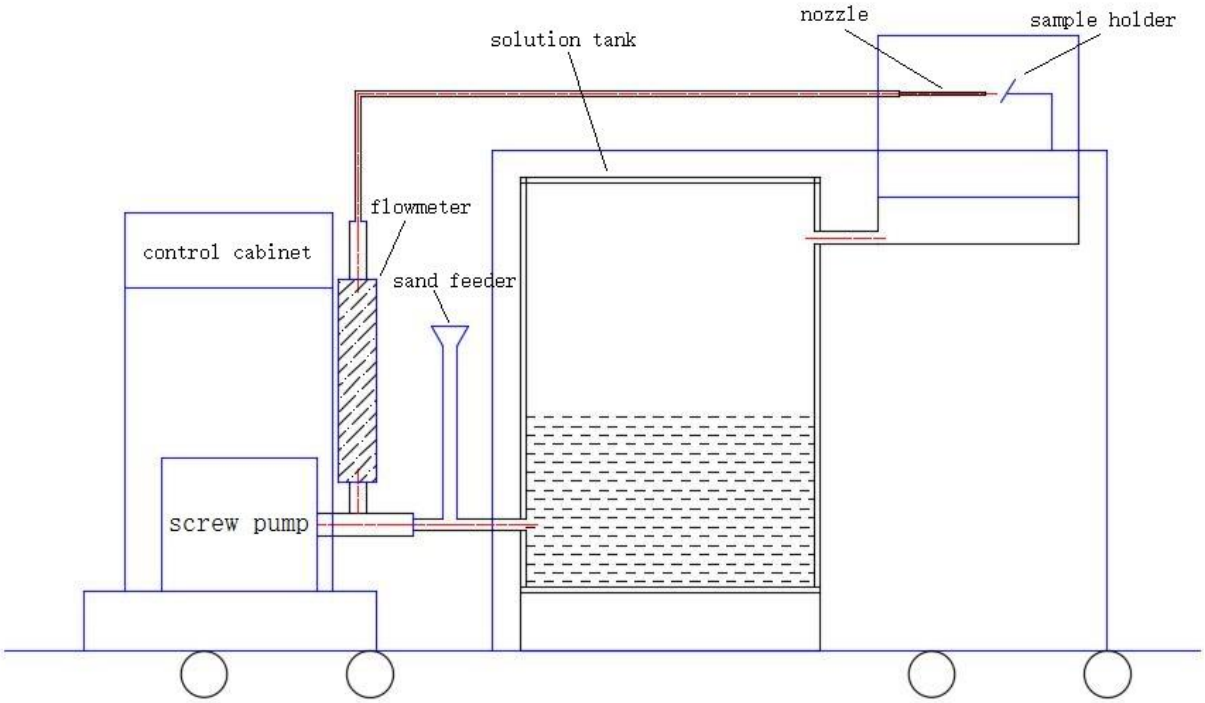

Figure 1. Schematic diagram of the water-sand erosion loop system

Table 1. Chemical composition of X65 pipeline steel (wt. %)

C	Si	Mn	P	S	Ni	Cr
0.09	0.26	1.30	0.007	0.002	0.15	0.04

Table 2. Chemical composition of the testing solution (g/L)

NaCl	KCl	$CaCl_2$	Na_2SO_4	$MgCl_2{\cdot}6H_2O$	$NaHCO_3$
90.44	2.20	17.32	0.43	6.33	0.49

3. NUMERICAL SIMULATION

3.1 Geometry and mesh models

According to the above experimental design, the geometry model for flowing jet and sample was created, as shown in Fig. 2a. The geometry model is composed of three parts. One part is labelled as Inlet and Wall-1, which is used to simulate the flowing jet. The second part is Wall-2, which is used to simulate the test sample, and the third part is labelled as Outlet, which is used to simulate the outer domain around test sample. For numerical simulations, the computational domain was discretized by using the hex dominant mesh method. After automatic mesh based defeaturing, a grid with 13520 nodes and 15377 elements was generated, as shown in Fig. 2b.

3.2 Mathematical model

The testing solution was composed of a continuous phase (water) and a discrete phase (sand). During the simulation, it was assumed that water was incompressible flow, and there was no heat exchange between the water and sand particles. For the continuous phase, the steady state Reynolds averaged Navier-Stokes (RANS) equations were used for modelling the turbulence. The continuity and time averaged-momentum conservation equations (dropping the overbar on the mean velocity $\bar{u}$) for the water phase are required to solve [14]:

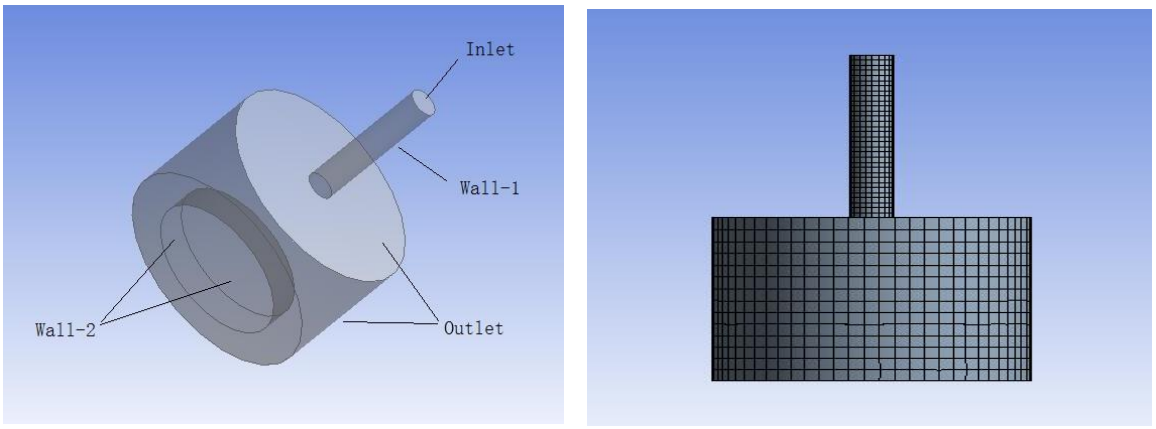

(a) Geometry model (b) Mesh model

Figure 2. Geometry and mesh models of the erosion system under the impingement angle of 90°

Continuity equation:

$$\frac{\partial \rho}{\partial t} + \frac{\partial}{\partial x_i}(\rho u_i) = 0 \quad (2)$$

Momentum equation

$$\frac{\partial}{\partial t}(\rho u_i) + \frac{\partial}{\partial x_j}(\rho u_i u_j) = -\frac{\partial p}{\partial x_i} + \frac{\partial}{\partial x_j}\left[\mu\left(\frac{\partial u_i}{\partial x_j} + \frac{\partial u_j}{\partial x_i} - \frac{2}{3}\delta_{ij}\frac{\partial u_l}{\partial x_l}\right)\right] + \frac{\partial}{\partial x_j}(-\rho\overline{u_i' u_j'}) \quad (3)$$

where ρ is density, u is velocity, p is the static pressure, and μ is viscosity of the water phase. The additional term$(-\rho\overline{u_i' u_j'})$, Reynolds stress, represented the effects of turbulence, and must be modelled to close Eq. (3). These Reynolds stresses were modelled by using the SST *k-ω* turbulent model. The

shear stress transport (SST), which is based on a blending of *k-ω* and *k-ε* turbulence models, was used to express the turbulent fluid flow in the inner region of the boundary layer, as well as in the outer part of boundary layer, for a wide range of Reynolds numbers [15, 16]. The transport equations for the SST *k-ω* model had the following forms [14]:

$$\frac{\partial}{\partial t}(\rho k) + \frac{\partial}{\partial x_i}(\rho k u_i) = \frac{\partial}{\partial x_j}(\Gamma_k \frac{\partial k}{\partial x_j}) + G_k - Y_k \quad (4)$$

$$\frac{\partial}{\partial t}(\rho \omega) + \frac{\partial}{\partial x_j}(\rho \omega u_j) = \frac{\partial}{\partial x_j}(\Gamma_\omega \frac{\partial \omega}{\partial x_j}) + G_\omega - Y_\omega + D_\omega \quad (5)$$

In these equations, the term G_k represented the production of the turbulence kinetic energy; G_ω represented the generation of ω; Γ_k and Γ_ω represented the effective diffusivity of k and ω, respectively; Y_k and Y_ω represented the dissipation of k and ω, respectively, due to turbulence; and D_ω represented the cross-diffusion term.

For the discrete phase, sand particles were tracked using the discrete phase model (DPM) in the Lagrangian frame of the reference where the particle trajectory was given as [10, 14]:

$$\frac{dx}{dt} = u_p \quad (6)$$

The trajectory of a discrete phase particle could be predicted by integrating the force balance on the particle in ANSYS Fluent software. This force balance equated the particle inertia, with the forces acting on the particle, and could be written as [14]:

$$\frac{du_p}{dt} = F_D(u - u_p) + \frac{g(\rho_p - \rho)}{\rho_p} + F_i \quad (7)$$

where F_i is an additional acceleration (force/unit particle mass) term, which included the virtual mass, Brownian force, Saffman's lift force, and thermophoretic force [17]. The second term is the gravity force acting on the sand particle, which strongly depended on the water-sand density difference. $F_D(u - u_p)$ is the drag force per unit particle mass, which depended on the water properties, particle geometry configuration, and sand-water velocity difference. F_D is defined as:

$$F_D = \frac{18\mu}{\rho_p d_p^2}\frac{C_D R_e}{24} \quad (8)$$

where u is the fluid phase velocity, u_p is the particle velocity, μ is the molecular viscosity of the fluid, ρ is the fluid density, ρ_p is the density of the particle, and d_p is the particle diameter. R_e is the relative Reynolds number, which is defined as:

$$R_e = \frac{\rho d_p |u_p - u|}{\mu} \quad (9)$$

The drag coefficient C_D as a function of the particle Reynolds number was defined by:

$$C_D = a_1 + \frac{a_2}{R_e} + \frac{a_3}{{R_e}^2} \quad (10)$$

where a_1, a_2, and a_3 were constants that were applied over various ranges of the Reynolds number given by Morsi and Alexander [18], which was suitable for spherical particles. In this study, the drag force was the dominant term. The additional acceleration term, F_i, was often much smaller than the drag force and could be neglected.

Particle erosion rates could be monitored at wall boundaries. The erosion rate was defined as [14, 19]:

$$R_{erosion} = \sum_{p=1}^{N_{particle}} \frac{\dot{m}_p C(d_p) f(\alpha) v^{b(v)}}{A_{face}} \quad (11)$$

where $C(d_p)$ was a function of particle diameter, α was the impact angle of the particle path with the

wall face, $f(\alpha)$ was a function of impact angle, v was the relative particle velocity, $b(v)$ was a function of the relative particle velocity, and A_{face} was the area of the cell face at the wall. When the impact angle is 90°, the function of the impact angle is equal to 0.4 [11]. The velocity exponent and the diameter functions were set to 2.6 and $1.8*10^{-9}$, respectively [20].

The type of solver was pressure-based, and the steady flow solver had been selected. In the parameter setting, the continuous phase was set to water, which was downloaded from the fluid database, and the density and viscosity of the water phase are ρ = 998.2 kg/m^3 and μ = $1.003*10^{-3}$ kg/(m·s), respectively. Similar to the sand used in erosion testing, the size and density of the particles was set to 300 μm and 2600 kg/m^3, respectively. The particle trajectories were tracked using a discrete random walk model [14, 21], which considered the effect of turbulent velocity fluctuations. The density of the wall face was set to 8030 kg/m^3, which is similar to the density of the test sample. The boundary condition of the inlet was set to velocity-inlet, which was suitable for incompressible flow. The outlet type was set to the outflow, which was generally used in a fully developed flow field. A convergence criterion of $1.0*10^{-5}$ was applied. Before calculation, the solution needed to be initialized.

The ANSYS fluent 14.5 software was used to simulate the erosion behaviour of the X65 pipeline steel under different flow velocities and sand concentrations. After post processing of the numerical simulation, the flow path, pressure contour and erosion rate distribution were obtained.

4. RESULTS AND DISCUSSION

4.1 Effect of the flow velocity

The streamline and static pressure contour of the erosion process under a flow velocity of 17 m/s and a sand concentration of 0.05% are shown in Fig. 3. It can be observed from Fig. 3 that the fully developed flow velocity occurs at the inside region of the outlet, which implies that the design length of the jet satisfies the requirement of a stable outlet flow.

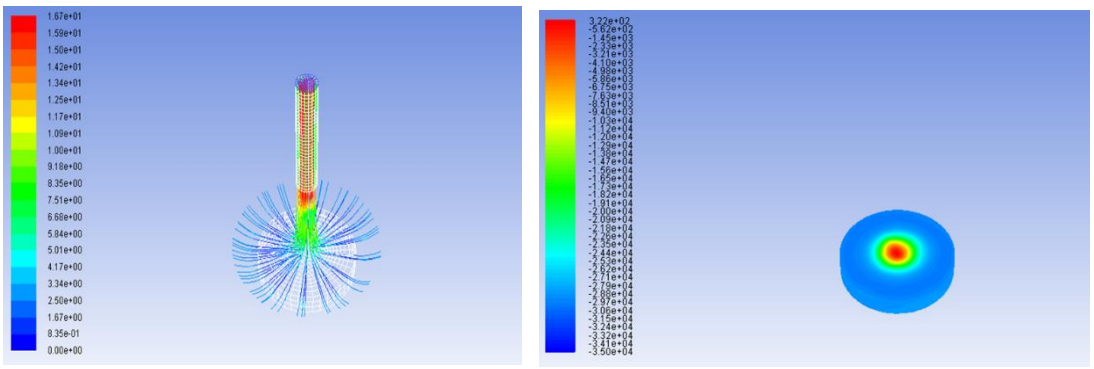

(a) streamline of water (b) contour of static pressure

Figure 3. Streamline and static pressure contour on the sample surface under a flowing velocity of 17 m/s and a sand concentration of 0.05%

In addition, the water phase diverges from the centre of the impact sample (Fig. 3a), which is in good agreement with the real water-sand erosion loop system in the experimental tests. From the centre to the periphery of the sample, the static pressure is continuously decreased (Fig. 3b). The maximum static pressure is located at the centre of the sample, which depends on the velocity of the water phase [10].

Fig. 4 is the distribution of the erosion rate of X65 pipeline steel by numerical simulation of the discrete phase model under different flow velocities with a sand concentration of 0.05 wt.%. It can be seen that the erosion of steel is located high in the range of -2.5 to 2.5 mm around the centre of the sample, which is in accord with the eroded surface after the experiments. Similar results have also been reported by Zhao [22] and Islam [23, 24]. The reason is that the sand particles that are away from the nozzle centre readily follow the fluid path lines due to dominance of the drag force over the inertia force of the sand particles, and this will reduce the protective effect of the film layer on the metal surface. It can also be concluded that the maximum erosion rate ($1.2*10^{-6}$, $2.3*10^{-6}$ and $3.4*10^{-6}$ $kg/m^2 \cdot s$ under the flow velocities of 11, 14 and 17 m/s, respectively) appeared in the centre of the sample and clearly increased with the increasing flow of velocity (Fig. 5). After the average, the erosion rate of steel under flow velocities of 11, 14 and 17 m/s are $3.97*10^{-7}$, $6.12*10^{-7}$ and $9.00*10^{-7}$ $kg/(m^2 \cdot s)$, respectively. These results are in general agreement with those reported in [12, 25, 26, 27]. From the point of view of the physical mechanism, on the one hand, the influence of the increasing velocity on the erosion rate can be associated with the impact of sand particles and the amount of energy transferred by each particle per impact. Both mechanisms can generate greater deformation, producing cracks and deep cuts on the surface and leading to increased material loss (as shown in Fig. 5). On the other hand, the increasing turbulence of the simulated formation water with the flow velocity also produces a disorientation of the particles with respect to the nominal direction expected for laminar flow, which further facilitates the removal of the material. From the point of view of the electrochemical mechanism, the increasing velocity can contribute to the erosion-corrosion rate by increasing the corrosion rate of the metallic target through mechanisms associated with flow-accelerated corrosion and erosion-enhanced corrosion [25]. The explanations proposed in previous papers [28-30] for these effects are mostly caused by the following: i) an increase in the mass-transfer coefficient of the electroactive species in the electrolyte to and from the electrode surface; ii) an increase in the surface roughness leading to an increment in the electrochemical activity of the metal by forming galvanic microcells on the surface of the material, thus allowing localized corrosion to take place; and iii) an increase in the oxygen concentration with increasing velocity at the metal interface implies an increase in the cathodic current, and the rate of corrosion is expected to rise [31].

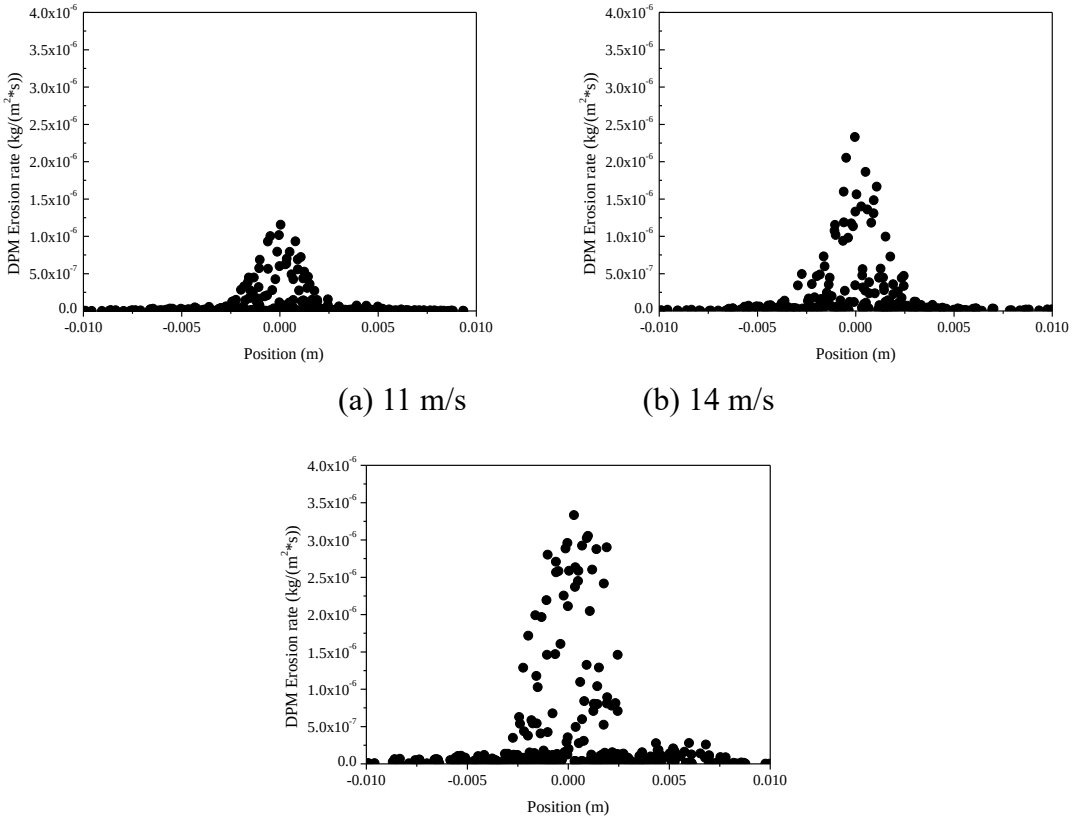

(a) 11 m/s (b) 14 m/s

(c) 17 m/s

Figure 4. Distribution of the erosion rate of X65 steel by DPM numerical simulation under different flow velocities with a sand concentration of 0.05%

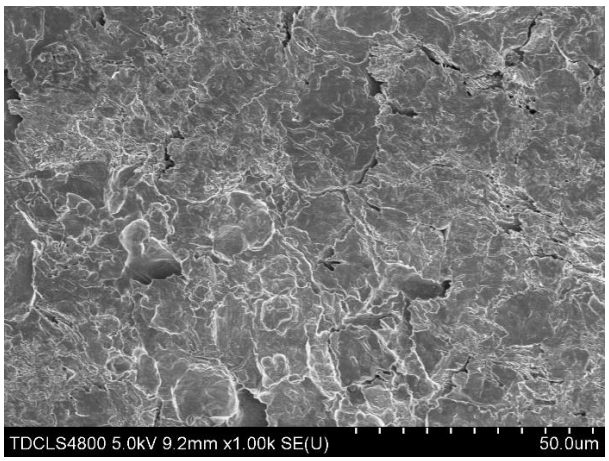

Figure 5. SEM photograph of the sample surface exposed to a simulated formation water solution mixed with 0.05 wt.% sands in a velocity of 14 m/s

The erosion rate of X65 steel under a continuous phase (CP rate) was determined in simulated formation water without sand particles and is shown in Table 3 and Fig. 6. From Table 3 and Fig. 6, it can be observed that the erosion rate by the continuous phase is also increased with the flow velocity, to about three or two times the erosion rate by the discrete phase (DPM rate) under the same flow velocity. By combining the erosion rates of the discrete phase and the continuous phase, the erosion rate of the

X65 steel under different flow velocity can be obtained, which is shown in Table 3 and Fig. 6.

The erosion rate of X65 steel by the experimental water-sand erosion loop system was measured and is shown in Table 3 and Fig. 6. The erosion rate by the experimental method is clearly increased with the flow velocity and is slightly smaller than the DPM+CP rate. All of these results implied that there is a good consistency between the experimental rate and the simulation rate, and the numerical simulation method is appropriate for the erosion of X65 steel in simulated formation water. Similar results were also reported by Nguyen et al. [12], Aguirre and Walczak [25]. The different values of the inlet velocity were used in both numerical simulations and experiments to investigate the effect of the impact velocity on both the erosion rate and the surface evolution. Similarly, a mixture of water and sand was perpendicularly sprayed onto the surface of the test sample. It was clearly seen that a higher erosion rate was caused by the increasing of flow velocity under the same concentration of sand particles. It can be seen from Fig. 6 that the numerical results have the same trend as the experimental data. Both numerical simulations and experiments confirm that the erosion rate is a linear function of average inlet velocity. However, it can also be seen that the numerical simulation is larger than the experimental data. On the one hand, this can be explained by the fact that the sand particle shape factor is maintained constant throughout the entire simulation process, while the sand particles in our experiment become rounded in the erosion process due to the recycle use of sand particles. Moreover, the particle-particle interaction might also occur in the experiments, but this interaction is not considered in the simulations. On the other hand, the sand particles are treated as ideal points; therefore, the actual psychical presence of a finite-sized particle was not considered. This can lead to errors in predicting the particle-particle interaction as well as the particle rebounding from the sample surface, thus reducing the accuracy in predicting the erosion rate [32].

Table 3. Comparison of the erosion rate by numerical simulation and experimental methods under different flow velocities

Flow velocity/m*s^{-1}	11	14	17
DPM rate	$3.97*10^{-7}$	$6.12*10^{-7}$	$9.00*10^{-7}$
CP rate	$1.39*10^{-6}$	$1.80*10^{-6}$	$2.10*10^{-6}$
DPM+CP rate	$1.79*10^{-6}$	$2.41*10^{-6}$	$3.00*10^{-6}$
Experimental rate	$1.75*10^{-6}$	$2.17*10^{-6}$	$2.57*10^{-6}$

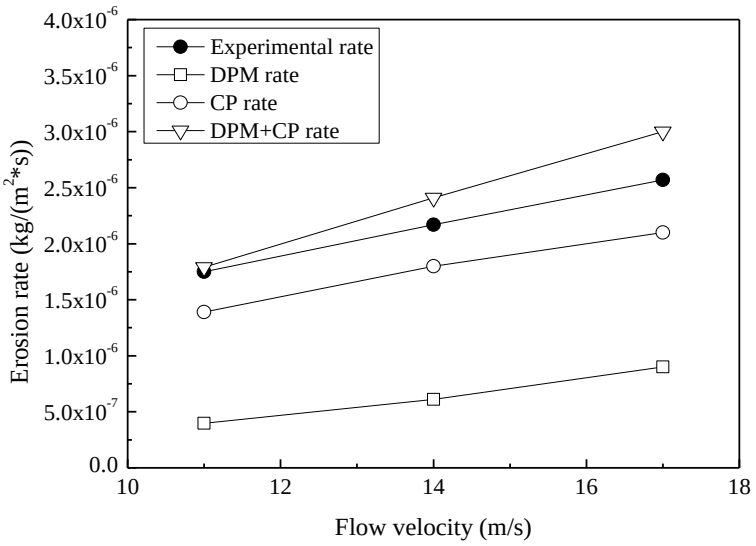

Figure 6. Erosion rate of X65 pipeline steel under different flow velocities

4.2 Effect of the sand concentration

The distribution of the erosion rate of X65 pipeline steel by the discrete phase model under different sand concentrations in the flow velocity of 11 m/s is shown in Fig. 7. It can be seen from Fig. 7 that the maximum erosion rate is located in the centre of the sample and increased from $1.2*10^{-6}$ kg/m^2·s (sand concentration 0.05%) to $1.7*10^{-6}$ kg/m^2·s (0.10%) and $3.5*10^{-6}$ kg/m^2·s (sand concentration 0.20%). Meanwhile, the radius of the eroded area increased from 0.0025 m (sand concentration 0.05%) to 0.005 m (sand concentration 0.20%). After the average, the erosion rates of steel under the sand concentrations 0.05%, 0.10% and 0.20% were $3.97*10^{-7}$, $7.9*10^{-7}$ and $1.41*10^{-6}$ kg/(m^2·s), respectively. These results are consistent with the research findings that were reported by other authors [33-36]. The sand particles could destroy the protective film on the material, thereby exposing the bare metal surface to the simulated formation water. The wear of the atoms on the metal surface accelerates with the increasing sand concentration. The impact, or abrasion, by sand particles is the dominant material removal mechanism [37,38].

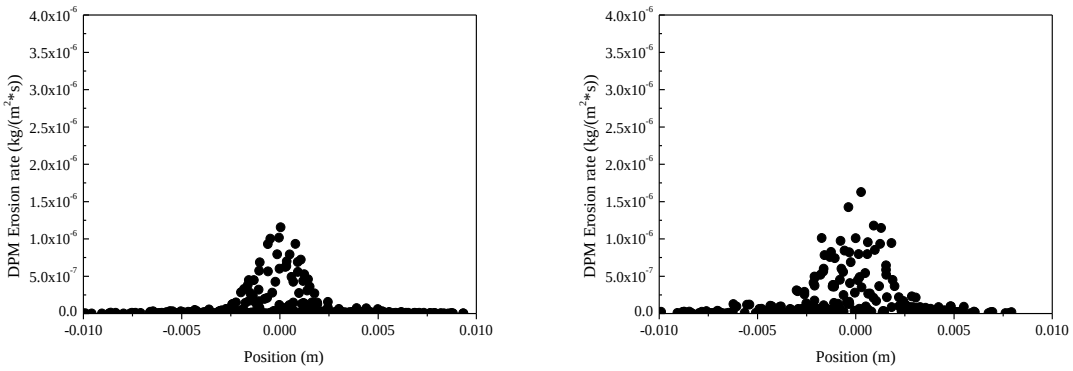

(a) 0.05 wt.% (b) 0.10 wt.%

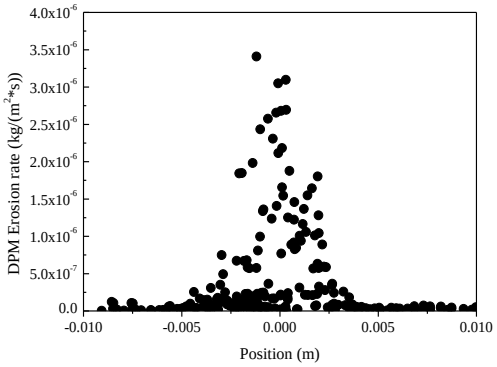

(c) 0.20 wt.%

Figure 7. Distribution of the erosion rate of X65 steel under different sand concentrations by numerical simulation

By considering that the erosion rate of the continuous phase (CP rate) under the flow velocity of 11 m/s is $1.39*10^{-6}$ kg/m^2·s, as shown in Table 3, the erosion rates under the continuous phase and the discrete phase are calculated and listed in Table 4. From Table 4, it can be seen that more erosion is caused by the discrete phase component (DPM rate) with the increasing sand concentration in the simulated formation water.

The erosion of X65 steel was tested in simulated formation water with different sand concentrations by using a water-sand erosion loop system, and the erosion rate was determined in Table 4 and Fig. 8. As shown in Table 4 and Fig. 8, the erosion rate of X65 steel clearly increased with the increasing sand concentrations, and the experimental erosion rate was nearly the same as the DPM+CP rate (Fig. 8) under different sand concentrations. It was observed that the numerical results also have the same trend as the experimental data. These results agree with previous observations [39].

From the above discussion, it can be concluded that for the erosion under different flow velocities or sand concentrations, the numerical simulation results have good consistency with the experimental erosion rate. Therefore, the numerical simulation method based on the geometry model, shear stress transport (SST) *k-ω* turbulence model and discrete phase model (DPM) is appropriate to simulate the erosion behaviour of the X65 pipeline steel in simulated formation water. In addition, there is an interaction between the flow velocity and the sand concentration. On the one hand, sand particles destroy metal surface and lead to material wear. On the other hand, the velocity of flow will accelerate the surface wear and increase the corrosion of fluid to the metal surface. Similar experimental results were reported by Rajahram [26], which indicated that at low velocities, the increasing sand concentration does not severely affect the erosion-corrosion rates, which indicates that the velocity has a more dominant effect. In this situation, although the number of sand particles is increased, there is insufficient kinetic energy to cause significant wear on the material. Above 8 m/s, the sand concentration starts to play a dominant role in the erosion-corrosion process, where the high number of sand particles within the medium with higher kinetic energy per particle produces more damage on the surface and can effectively remove the oxide film to cause high erosion and corrosion rates.

Table 4. Comparison of the erosion rate by numerical simulation and experimental methods under different sand concentrations

Sand concentration/ wt.%	0.05	0.10	0.20
DPM rate	$3.97*10^{-7}$	$7.90*10^{-7}$	$1.41*10^{-6}$
CP rate	$1.39*10^{-6}$	$1.39*10^{-6}$	$1.39*10^{-6}$
DPM+CP rate	$1.79*10^{-6}$	$2.18*10^{-6}$	$2.80*10^{-6}$
Experimental rate	$1.75*10^{-6}$	$2.20*10^{-6}$	$2.91*10^{-6}$

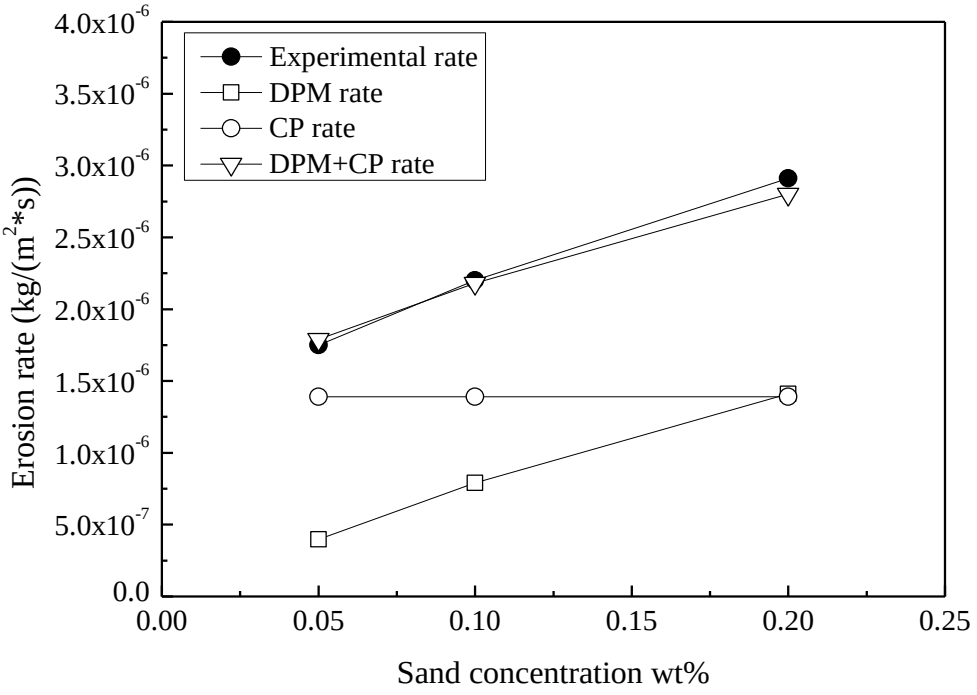

Figure 8. Erosion rate of X65 pipeline steel under different sand concentrations

5. CONCLUSIONS

(1) With the increasing of flow velocity, the erosion rate of X65 pipeline steel in simulated formation water is clearly increased, and the erosion rates under the discrete phase and the continuous phase are both enhanced. Whereas the erosion rate of X65 pipeline steel, especially the erosion rate under the discrete phase, is increased rapidly with the increasing sand concentrations in simulated formation water.

(2) The erosion behaviour is simulated by using a geometry model, SST k-ω turbulence model and DPM model. Furthermore, there is a good agreement between the numerical simulation erosion rate and the experimental results.

ACKNOWLEDGEMENT
This work was jointly supported by National Natural Science Foundation of China (No. 51771133), the National Basic Research Program of China (No. 2014CB046801) and the Key Project of Tianjin Natural Science Foundation (No. 13JCZDJC29500).

References

1. I. Finnie, D. H. McFadden, *Wear*, 48(1978)181-190.
2. S. Turenne, M. Fiset, J. Masounave, *Wear*, 133(1989)95-106.
3. Y. I. Oka, H. Ohnogi, T. Hosokawa, M. Matsumura, *Wear*, 203(1997)573-579.
4. R. S. Lynn, K. K. Wong, H. M. I. Clark, *Wear*, 149(1991)55-71.
5. A. V. Levy, P. Chik, *Wear*, 89(1983)151-162.
6. A. H. Azimi, D. Z. Zhu, N. Rajaratnam, *International Journal of Multiphase Flow*, 40 (2012)19-37.
7. G. A. Zhang, L. Y. Xu, Y. F. Cheng, *Corrosion Science*, 51(2009)283-290.
8. L. Niu, Y. F. Cheng, *Wear*, 265(2008)367-374.
9. M. M. Stack, G. H. Abdulrahman, *Tribology International*, 43(2010)1268-1277.
10. H. S. Grewal, H. Singh, E. S. Yoon, *Wear*, 332(2015)1111-1119.
11. S. Shamshirband, A. Malvandi, A. Karimipour, M. Goodarzi, M. Afrand, D. Petković, M. Dahari, N. Mahmoodian, *Powder Technology*, 284(2015)336-343.
12. V. B. Nguyen, Q. B. Nguyen, Z. G. Liu, S. Wan, C. Y. H. Lim, Y. W. Zhang, *Wear*, 319(2014)96-109.
13. L. Zeng, G. A. Zhang, X. P. Guo, *Corrosion Science*, 85(2014)318-330.
14. ANSYS Fluent Theory Guide, ANSYS Inc., Southpoint, 275 Technology drive, Canonburg, PA 15317, USA.
15. V. B. Nguyen, H. J. Poh, Y. W. Zhang, *Powder Technology*, 256(2014)100-112.
16. F. R. Menter, *AIAA journal*, 32(1994)1598-1605.
17. P. G. T. Saffman, *Journal of Fluid Mechanics*, 22(1965)385-400.
18. S. A. Morsi, A. J. Alexander, *Journal of Fluid Mechanics*, 55(1972)193-208.
19. A. Campos-Amezcua, A. Gallegos-Muñoz, C. A. Romero, Z. Mazur-Czerwiec, R. Campos-Amezcua, *Applied Thermal Engineering*, 27(2007)2394-2403.
20. A. Gnanavelu, N. Kapur, A. Neville, J. F. Flores, N. Ghorbani, *Wear*, 271(2011)712-719.
21. A. Haider, O. Levenspiel, *Powder Technology*, 58(1989)63-70.
22. W. M. Zhao, C. Wang, T. M. Zhang, M. Yang, B. Han, A. Neville, *Wear*, 362-363(2016)39-52.
23. M. A. Islam, Z. N. Farhat, E. M. Ahmed, A. M. Alfantazi, *Wear*, 302(2013)1592-1601.
24. M. A. Islam, Z. N. Farhat, *Tribology International*, 68(2013)26-34.
25. J. Aguirre, M. Walczak, *Tribology International*, (2018), doi: 10.1016/j.triboint.2018.04.029.
26. S.S. Rajahram, T. J. Harvey, R. J. K. Wood, *Tribology International*, 43(2010)2072-2083.
27. J.Z. Yi, H.X. Hua, Z.B. Wang, Y.G. Zheng, *Wear*, 416-417(2018)62-71.
28. S. Zhou, M. M. Stack, R.C. Newman, *Corrosion Science*, 52(1996)934-946.
29. B. T. Lu, J. L. Luo, *Journal of Physical Chemistry B*, 110(2006)4217-4231.
30. J. H. Xie, A. T. Alpas, D. O. Northwood, *Journal of Materials Science*, 38.24(2003)4849-4856.
31. J. Jiang, Y. Xie, M. A. Islam, M. M. Stack, *Journal of Bio- and Tribo-Corrosion*, 3(2017)45.
32. A. Gnanavelu, N. Kapur, A. Neville, J. F. Flores, N. Ghorbani, *Wear*, 271(2011)712-719.
33. C.G. Telfer, M.M. Stack, B. D. Jana, *Tribology International*. 53 (2012)35-44.
34. H.X. Hu, Y.G. Zheng, *Wear*, 384(2017)95-105.
35. R. Elemurena, R. Evittsb, I. Oguochaa, G. Kennellb, R. Gerspacherb, A. Odeshia, *Wear,* 410-411 (2018)149-155.
36. W.J. Gou, H. Zhang, H.P. Lia, F. Liu, J.J. Lian, *Wear,* 412-413(2018)120-126.

37. Y. Wang, Z.Z. Xing, Q. Luo, A. Rahman, J. Jiao, S.J. Qu, Y.G. Zheng, J. Shen, *Corrosion Science*, 98(2015)339-353.
38. S.R. Li, Y. Zuo, P. Ju, *Applied Surface Science*, 331(2015)200-209.
39. V. B. Nguyen, Q. B. Nguyen, Y. W. Zhang, C. Y. H. Lim, B. C. Khoo, *Wear*, 348-349(2016)126-137.